

# Performance of Medical Image Fusion in High-level Analysis Tasks: A Mutual Enhancement Framework for Unaligned PAT and MRI Image Fusion

Yutian Zhong<sup>a,b,c</sup>, Jinchuan He<sup>a,b,c</sup>, Zhichao Liang<sup>a,b,c</sup>, Shuangyang Zhang<sup>a,b,c</sup>, Qianjin Feng<sup>a,b,c</sup>, Wufan Chen<sup>a,b,c</sup>, Li Qi<sup>a,b,c,\*</sup>

<sup>a</sup>School of Biomedical Engineering, Southern Medical University, Guangzhou, China

<sup>b</sup>Guangdong Provincial Key Laboratory of Medical Image Processing, Southern Medical University, Guangzhou, China

<sup>c</sup>Guangdong Province Engineering Laboratory for Medical Imaging and Diagnostic Technology, Southern Medical University, Guangzhou, China

## ARTICLE INFO

Article history:

2000 MSC: 41A05, 41A10, 65D05, 65D17

Keywords: Photoacoustic tomography, Magnetic resonance imaging, Image fusion, High-level analysis task

## ABSTRACT

Photoacoustic tomography (PAT) offers optical contrast, whereas magnetic resonance imaging (MRI) excels in imaging soft tissue and organ anatomy. The fusion of PAT with MRI holds promising application prospects due to their complementary advantages. Existing image fusion have made considerable progress in pre-registered images, yet spatial deformations are difficult to avoid in medical imaging scenarios. More importantly, current algorithms focus on visual quality and statistical metrics, thus overlooking the requirements of high-level tasks. To address these challenges, we proposes a unsupervised fusion model, termed PAMRFuse+, which integrates image generation and registration. Specifically, a cross-modal style transfer network is introduced to simplify cross-modal registration to single-modal registration. Subsequently, a multi-level registration network is employed to predict displacement vector fields. Furthermore, a dual-branch feature decomposition fusion network is proposed to address the challenges of cross-modal feature modeling and decomposition by integrating modality-specific and modality-shared features. PAMRFuse+ achieves satisfactory results in registering and fusing unaligned PAT-MRI datasets. Moreover, for the first time, we evaluate the performance of medical image fusion with contour segmentation and multi-organ instance segmentation. Extensive experimental demonstrations reveal the advantages of PAMRFuse+ in improving the performance of medical image analysis tasks.

© 2024

## 1. Introduction

In biomedical imaging, photoacoustic tomography (PAT) and magnetic resonance imaging (MRI) represent two advanced imaging modalities. PAT as an emerging biomedical imaging technique combines the high contrast of optical imaging with the deep imaging range of ultrasound, enabling the visualization of fine structures and tissue characteristics (Wang and Yao, 2016; Wang and Hu, 2012; Lin et al., 2021; Huda et al., 2023). In contrast, MRI is a mature medical imaging technology that

utilizes magnetic fields and radio waves to provide excellent soft tissue contrast (Zhang et al., 2022). Although PAT can provide functional and molecular information about tissues, it is limited by tissue optical scattering and lacks soft tissue contrast. Conversely, MRI can offer good soft tissue information, but its temporal resolution is limited. This complementarity motivates us to integrate the unique information between PAT and MRI images to obtain more comprehensive and accurate information.

Many existing approaches for integrating PAT and MRI information primarily rely on hardware or registration techniques. For instance, Gehring et al. (Gehring et al., 2020) pioneered the use of a custom-made disposable silicone MRI

\*Corresponding author  
e-mail: qili@smu.edu.cn (Li Qi)

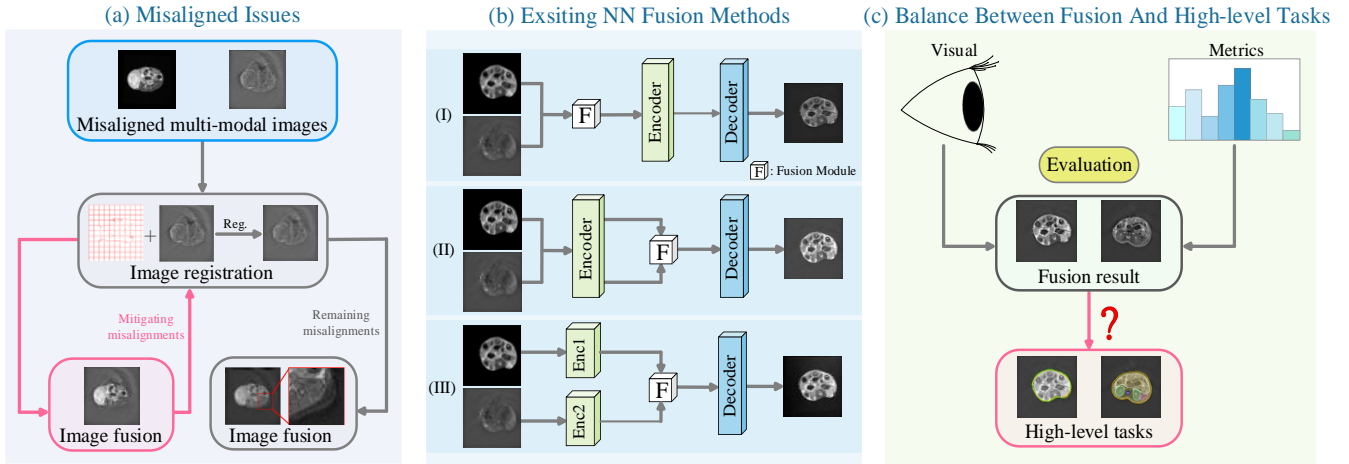


**Fig. 1. Image fusion methods face some pressing challenges. (a) Misalignment of source images leads to artifacts in the fusion results. Reg.=Registration. (b) Existing fusion methods fail to produce higher-quality fusion images. (c) In terms of evaluation, current fusion methods overlook adaptability to advanced visual tasks.**

holder to register abdominal PAT and MRI images of small animals, introducing a series of parallel PAT-MRI imaging systems (Ren et al., 2021; Chen et al., 2022). Recently, researchers have increasingly focused on developing deep learning (DL)-based registration algorithms (Ni et al., 2022; Hu et al., 2021). Compared to previous manual registration methods (Ni et al., 2018b,a), DL-based methods offer higher efficiency and better handling of image deformations. However, these methods have yet to achieve true information fusion. The goal of image fusion is to extract valuable information from each image and combine them into a single image with more comprehensive information and improved visualization.

Image fusion has attracted significant attention due to its advantages. Over the past few decades, numerous image fusion techniques have been proposed, encompassing both traditional methods and DL-based methods. Traditional methods are commonly categorized into the following groups: multi-scale transformation (MST) (Liu et al., 2014), sparse representation (SR) (Li et al., 2020b), subspace-based methods (Cvejic et al., 2007), optimization-based methods (Ma et al., 2016), and hybrid methods (Ma et al., 2017). However, these manually designed methods not only entail complexity and time consumption but also often overlook differences in feature representation between different image modalities. In recent years, the emergence of several DL-based fusion methods has been observed, such as frameworks utilizing autoencoders (AE) (Li and Wu, 2019; Li et al., 2020a), convolutional neural networks (CNN) (Zhang et al., 2020; Ma et al., 2021), and generative adversarial networks (GAN) (Ma et al., 2020; Zhang et al., 2021a). Due to its practical applicability, image fusion finds wide-ranging applications in the medical imaging domain, including CT-MRI, CT-PET, MRI-PET, etc. Our group recently introduced the PAMRFuse network (Zhong et al., 2024) which achieves PAT and MRI fusion. Despite the capability of the PAMRFuse network to generate good fusion images, there remain pressing challenges in the field of PAT and MRI image fusion.

Firstly, existing fusion methods do not account for image misalignments. When the source images are misaligned, this

leads to noticeable artifacts in the fusion results, as shown in Fig.1 (a). Therefore, fusion methods need to employ multi-modal image registration as a preprocessing step to alleviate misalignments. Unfortunately, the diversity between different modalities poses significant challenges to improving registration accuracy. Secondly, registration and fusion are usually treated as two independent issues, with image fusion being a downstream task. In fact, misaligned regions in the input images lead to repeated prominent structures, while accurate registration facilitates gradient sparsity. Thus, gradient sparsity may serve as a criterion for feedback and improve registration accuracy. Moreover, more accurate alignment data will further enhance fusion results.

Secondly, regarding the challenges of image fusion, methods based on CNN for feature extraction and fusion have many shortcomings. As a basic operation, CNN are difficult to control and interpret, leading to inadequate extraction of cross-channel features. For example, in Fig.1 (b), the shared encoder in (i) and (ii) fails to distinguish modality-specific features, while the private encoder in (iii) overlooks features shared between modalities.

Thirdly, as shown in Fig.1 (c), existing fusion algorithms tend to prioritize enhancing visual quality and evaluation metrics, such as sharpness, contrast, and structural preservation, while neglecting the adaptability of fused images for high-level tasks. To ensure accuracy and reliability of these tasks, the fused images should not only have good visual quality but also retain the semantic information and structural features of the original images. Therefore, the development of image fusion algorithms suitable for high-level visual tasks is of paramount importance, necessitating a balance between improving the visual quality of fused images and considering the adaptability and effectiveness for various high-level tasks.

High-level tasks can be considered as the concrete utilization of information contained within images, which is indispensable in medical imaging analysis. Specifically, in the application of PAT, effective contour segmentation can differentiate imaging tissue regions from surrounding coupling media (such as

water), which is crucial for describing anatomical features and identifying spatial optical characteristics (Liang et al., 2022). Additionally, tissue or organ segmentation is often a prerequisite for the region of interest analysis and molecular imaging, where effective segmentation assists in computing biomarker concentrations (Lauri et al., 2019), quantitative analysis of blood vessels (Sun et al., 2020) and estimating and correcting the effects of internal light attenuation, thereby achieving quantitative imaging (Yuan and Jiang, 2006). Unfortunately, due to insufficient resolution and contrast of existing imaging technologies, the segmentation performance of PAT images is suboptimal (Liang et al., 2022). There is a pressing need for an effective auxiliary technique that preserves the advantages of PAT images while meeting the requirements of segmentation and its associated advanced visual tasks.

To address the limitations of previous work and unexplored issues, we propose for the first time the use of image fusion to enhance advanced visual tasks in PAT, and achieve multimodal PAT-MRI image synthesis, registration, and fusion within a mutually reinforcing framework. We introduce an unsupervised network to achieve this, named PAMRFuse+. We introduce a cross-modal generation-registration paradigm for alignment of PAT-MRI images. Specifically, we propose a generation network P2M, capable of generating pseudo-MRI images from PAT images, which facilitates single-modal registration between real MRI images and the generated pseudo-MRI images. We then utilize a multi-level registration network (MLR) to predict deformation fields between MRI and pseudo-MRI images from coarse to fine. Subsequently, PAMRFuse+ explores a rational paradigm to address challenges in feature extraction and fusion by proposing a dual-branch feature decomposition fusion (DFDF) model, which achieves modality-specific and modality-shared feature extraction by dual-branch encoders and fused image reconstruction by decoders. We evaluate the proposed method on unaligned PAT-MRI datasets, achieving excellent performance in both image registration and fusion simultaneously. More crucially, we assess the effects of image fusion in advanced visual tasks such as contour segmentation and multi-organ instance segmentation, where PAMRFuse+ shows its potential to facilitate performance in advanced visual tasks.

The main contributions of this paper are summarized as follows:

1. We propose for the first time the use of image fusion to enhance advanced analysis tasks in PAT and introduce a highly robust unsupervised PAT and MRI image fusion framework.
2. We develop a generation-registration paradigm to overcome the difficulty of cross-modal source image alignment.
3. For the fusion network, we propose a dual-branch transformer framework for extracting and fusing modality-specific and modality-shared features.
4. We employ a task-driven evaluation approach to assess the performance of image fusion from the perspectives of contour segmentation and multi-organ instance segmentation. To our knowledge, this is the first time that advanced tasks have been used to evaluate the effectiveness of medical image fusion.

## 2. Methods

In this section, we provide a comprehensive description of the PAT and MRI image fusion framework, PAMRFuse+. Firstly, we introduce the overall framework consisting of image synthesis, registration, and fusion modules. Next, we provide detailed descriptions of each module, including their internal pipelines and network architectures. Finally, we present the training strategy and loss functions employed in this study.

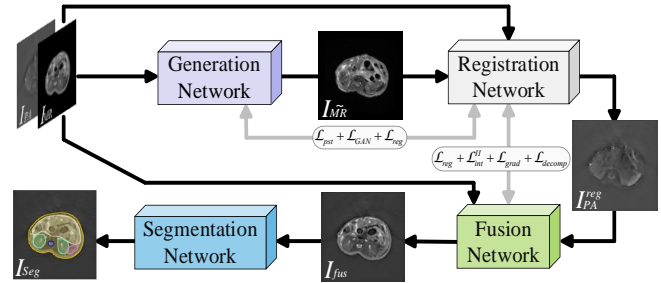


Fig. 2. The overall network architecture of PAMRFuse+.

### 2.1. Overall framework

Given a set of unaligned PAT images and MRI images, our goal is to enhance the performance of advanced visual tasks by synthesizing, registering, and reconstructing fused images of PAT and MRI using our end-to-end image fusion network (PAMRFuse+) under the guidance of a customized loss function. As depicted in Fig.2, the entire process is divided into three main stages. Firstly, different imaging modalities and sensors may result in misalignments observed between the PAT and MRI images, manifested as shifts and deformations. The direct fusion of unaligned PAT and MRI images often leads to severe artifacts (Zhong et al., 2024). Inspired by Wang et al.'s approach (Wang et al., 2019) of reducing differences between multimodalities through image synthesis, we propose a cross-modal synthesis-registration paradigm to mitigate artifacts during PAT and MRI image fusion. Specifically, our cross-modal image synthesis network (P2M) captures information shared across multiple modalities, taking PAT images as input and outputting pseudo-MRI images with clear structures. It aids in simplifying the multimodal registration challenge into monomodal registration. Secondly, fine registration is conducted using a multi-level registration network. Representations extracted by the image synthesis network establish registration constraints, and these constraints are then utilized to predict deformation fields for misaligned MRI and pseudo-MRI images. Finally, the dual-branch feature decomposition fusion model integrates information from source images. DFDF achieves modality-specific and modality-shared feature extraction through dual-branch encoders, and the fused image is reconstructed by decoders.

### 2.2. Cross-modality Style Transfer

One inherent characteristic of PAT images is the emphasis on texture details rather than sharp geometric structures. To mitigate the low contrast issue caused by scattering in PAT images,

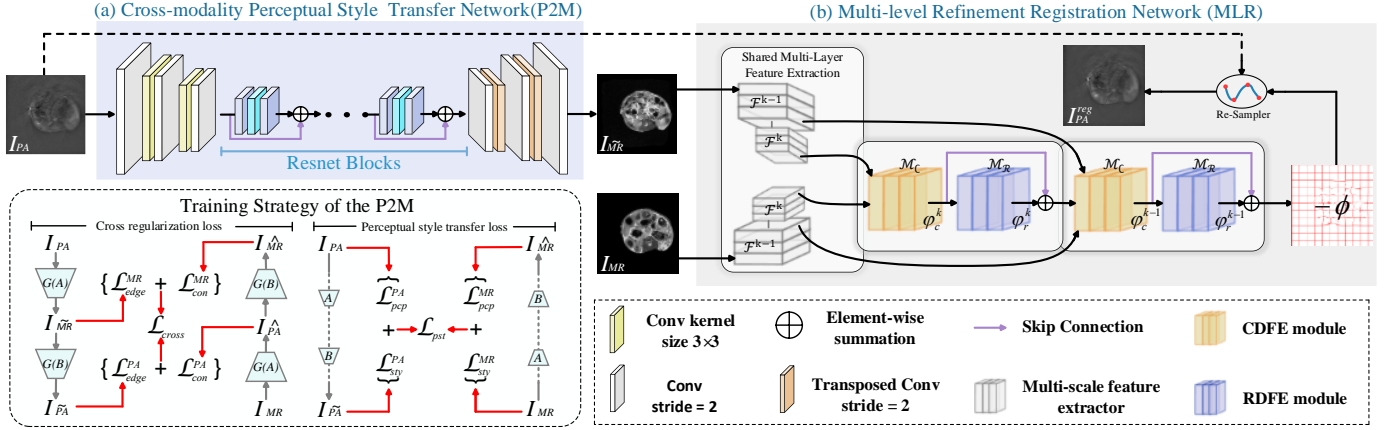


**Fig. 3.** The workflow of the cross-modal synthesis-registration paradigm. This method takes unregistered PAT and MRI images as input and processes them sequentially through the two sub-networks to obtain registered PAT images.

generating pseudo-MRI images with clear structural information is more advantageous for monomodal registration. Therefore, we propose a cross-modal style transfer network (P2M) to extract accurate geometric structures during the generation of pseudo-MRI images  $I_{MR}^{\sim}$  from PAT images  $I_{PA}$ , as depicted in Fig.3 (a). P2M is a generator similar to U-Net, consisting of 9 RESNET blocks (He et al., 2016). This network inherits the cycle-consistent learning approach from CycleGAN (Zhu et al., 2017). However, unlike CycleGAN, we aim to design a specific learning strategy controlled by perceptual style transfer constraints to further optimize the generation of pseudo-MRI images with sharp structures, laying the foundation for monomodal registration of MRI images. The regularization of perceptual style transfer constraints will be explained in Section 2.6.

### 2.3. Multi-level Refinement Registration

Due to the reduction of modality differences by P2M, monomodal image registration becomes another core aspect of the cross-modal synthesis-registration paradigm. As illustrated in Fig.3 (b), we employ a multi-level registration network to predict the deformation field between MRI images and pseudo-MRI images, and reconstruct the registered PAT image. MLR consists of a shared multi-layer feature extraction module, two coarse-to-fine deformation field estimation modules, and a resampling layer. Each coarse-to-fine deformation field estimation module includes a coarse deformation field estimation (CDFE) module  $\mathcal{M}_C$  and a refined deformation field estimation (RDDE) module  $\mathcal{M}_R$ . Subsequently, the coarse deformation field is predicted as follows:

$$\varphi_c^k = \mathcal{M}_C(\mathcal{F}^k(I_{MR}^{\sim}, I_{MR})) \quad (1)$$

where  $\mathcal{F}^k$  represents the  $k$ -th level feature extraction module. The estimation formula for the refined deformation field is:

$$\varphi_r^k = \mathcal{M}_R(\varphi_c^k) \oplus \varphi_c^k \quad (2)$$

Assuming the layer feature extraction module consists of  $K$  layers, when  $k = K$ , the final estimated deformation field is

$\phi = -\varphi_r^k$ . Finally, we use the resampling layer to reconstruct the registered PAT images:

$$I_{PA}^{reg} = I_{PA} \circ (\phi) \quad (3)$$

The operator  $\circ$  denotes the spatial transformation.

### 2.4. Dual-Branch Feature Decomposition Fusion

Our work explores a rational paradigm to address the challenges in PAT-MRI feature extraction and fusion. Initially, we impose correlation constraints on the extracted features to enhance the controllability and interpretability of feature extraction. We assume that the input features of the two modalities are correlated at low frequencies, representing shared information between modalities, while high-frequency features are uncorrelated, representing the unique features of each modality. Specifically, since PAT and MRI images come from the same imaging object, the low-frequency information of both modalities includes overall tissue morphology and approximate organ positions. In contrast, the high-frequency information of both modalities is independent, such as optical absorption information in PAT images and soft tissue structural information in MRI images. Therefore, our objective is to promote the extraction of modality-specific features and shared features by respectively increasing and decreasing the correlation between low-frequency and high-frequency features. Thus, we propose the dual-branch feature decomposition fusion model. In this section, we first introduce the workflow of DFDF and the detailed structure of each module. For simplicity, we represent low-frequency features as base features and high-frequency features as detail features.

#### 2.4.1. Overview

The specific workflow is illustrated in Fig.4 (a). DFDF consists of four modules, namely the dual-branch encoder for feature extraction and decomposition, the decoder for reconstructing the original image (in training stage I) or generating the fused image (in training stage II), and the basic/detail fusion layer for merging features of different frequencies. The two-stage training strategy will be explained in Section 2.5.

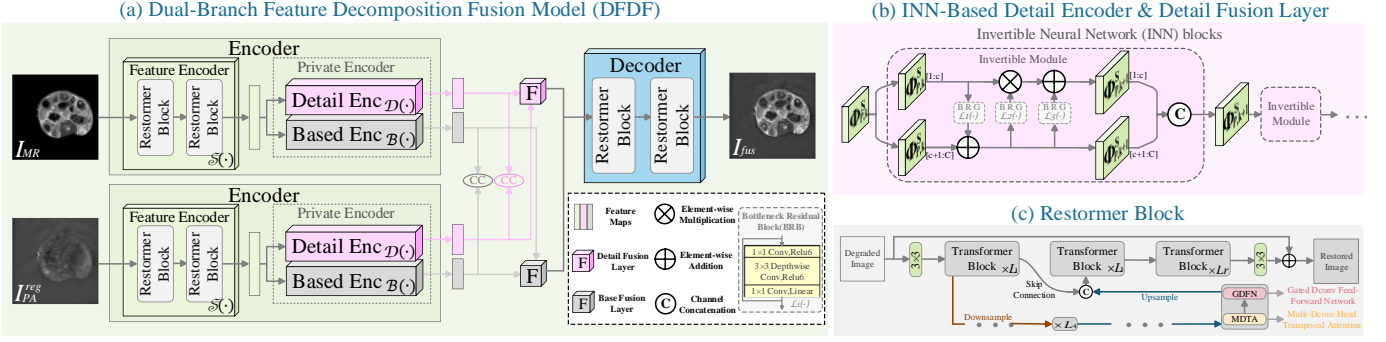


**Fig. 4.** (a) The workflow of the proposed DFDF module, which consists of three parts: encoder, fusion layer, and decoder. (b) The workflow of the detail information processing module. (c) The Restormer module used in the encoder and the decoder

#### 2.4.2. Encoder

The dual-branch encoder consists of three components: the feature encoder (FE) based on Restormer blocks (Zamir et al., 2022), the base encoder (BE) based on lite transformer blocks (LT) (Wu et al., 2020), and the detail encoder (DE) based on invertible neural network (INN) blocks (Dinh et al., 2017). The BE and DE together constitute the long-short distance encoder. For clarity of expression, we define some symbols. The paired PAT and MRI images are denoted as  $P \in \mathbb{R}^{H \times W}$  and  $M \in \mathbb{R}^{H \times W}$  respectively. The FE, BE, and DE are represented by  $\mathcal{S}(\cdot)$ ,  $\mathcal{B}(\cdot)$ , and  $\mathcal{D}(\cdot)$  respectively.

*Feature encoder.* The objective of FE is to extract shallow features  $\{\Phi_P^S, \Phi_M^S\}$  from the input PAT and MRI images  $\{P, M\}$ .

$$\Phi_P^S = \mathcal{S}(P), \quad \Phi_M^S = \mathcal{S}(M). \quad (4)$$

The reason for choosing Restormer blocks in FE is that the Restormer block can extract global features from input images by applying self-attention mechanisms across feature dimensions. The architecture of the Restormer block can be referenced in Fig.4 (c).

*Base encoder.* BE extracts low-frequency basic features from shared features:

$$\Phi_P^B = \mathcal{B}(\Phi_P^S), \quad \Phi_M^B = \mathcal{B}(\Phi_M^S). \quad (5)$$

The basic features of P and M are denoted as  $\Phi_P^B$  and  $\Phi_M^B$  respectively. In order to extract long-range dependent features, we employ a transformer with spatial self-attention. For a balance between performance and computational efficiency, we utilize the LT block as the basic unit of BE.

*Detail encoder.* In contrast to BE, DE extracts high-frequency detailed information from shared features:

$$\Phi_P^D = \mathcal{D}(\Phi_P^S), \quad \Phi_M^D = \mathcal{D}(\Phi_M^S). \quad (6)$$

Considering the importance of edge and texture information in the detail features for image fusion tasks, we aim for DE to retain as much detail information as possible. The INN module can be regarded as a lossless feature extraction module, highly suitable for this context. In each reversible layer, the transformation is as follows:

$$\begin{aligned} \Phi_{P,k+1}^S [c+1:C] &= \Phi_{P,k}^S [c+1:C] + \mathcal{L}_1(\Phi_{P,k}^S [1:c]), \\ \Phi_{P,k+1}^S [1:c] &= \Phi_{P,k}^S [1:c] \odot \exp(\mathcal{L}_2(\Phi_{P,k+1}^S [c+1:C])) \\ &\quad + \mathcal{L}_3(\Phi_{P,k+1}^S [c+1:C]), \\ \Phi_{P,k+1}^S &= \mathcal{CAT}(\Phi_{P,k+1}^S [1:c], \Phi_{P,k+1}^S [c+1:C]). \end{aligned} \quad (7)$$

Here,  $\odot$  denotes the Hadamard product,  $\Phi_{P,k}^S [1:c] \in \mathbb{R}^{h \times w \times c}$  represents the first to  $C$  channels of the input features of the  $k$ -th reversible layer ( $k = 1, \dots, K$ ),  $\mathcal{CAT}(\cdot)$  denotes channel-wise concatenation operation, and  $\mathcal{L}_i$  ( $i = 1, \dots, 3$ ) stands for the mapping function. Considering the balance between computational cost and feature extraction capability, we employ bottleneck residual blocks (Sandler et al., 2018) as  $\mathcal{L}_i$ . Finally,  $\Phi_P^D = \Phi_{P,k}^D$  and  $\Phi_M^D$  can be obtained using the same approach by replacing the subscript from  $P$  to  $M$ . Details of the calculations are shown in Fig.4 (b).

#### 2.4.3. Fusion layer

The function of the basic/detail fusion layer is to merge the basic/detail features separately. Considering that the basic/detail feature fusion should be similar to the basic/detail feature extraction in the encoder, we use LT and INN blocks as the basic and detail fusion layers, respectively, where:

$$\Phi^B = \mathcal{F}_B(\Phi_P^B, \Phi_M^B), \quad \Phi^D = \mathcal{F}_D(\Phi_P^D, \Phi_M^D). \quad (8)$$

$\mathcal{F}_B$  and  $\mathcal{F}_D$  are the basic fusion layer and detail fusion layer, respectively.

#### 2.4.4. Decoder

In the decoder  $\mathcal{DC}(\cdot)$ , the decomposed features are concatenated along the channel dimension as input, and the original image (during training phase I) or the fused image (during training phase II) is the output of the decoder, expressed by the following formula:

$$\begin{aligned} \text{Stage I: } \hat{I} &= \mathcal{DC}(\Phi_P^B, \Phi_P^D), \quad \hat{V} = \mathcal{DC}(\Phi_M^B, \Phi_M^D); \\ \text{Stage II: } F &= \mathcal{DC}(\Phi^B, \Phi^D). \end{aligned} \quad (9)$$

As the input here involves cross-channel and multi-frequency features, we maintain consistency in the design of the decoder with that of the FE by using Restormer blocks as the basic units.

## 2.5. Two-stage training

Existing multi-task model optimization paradigms either utilize pretrained high-level models to guide the training of low-level task models or jointly train multi-task models in a single stage. However, in the field of image fusion, it is challenging to provide ideal fusion images for training models. Additionally, single-stage joint training strategies may lead to difficulties in maintaining performance balance among multi-task models. Therefore, we have designed a two-stage training learning scheme for joint adaptive training of our network, as illustrated in Fig.5.

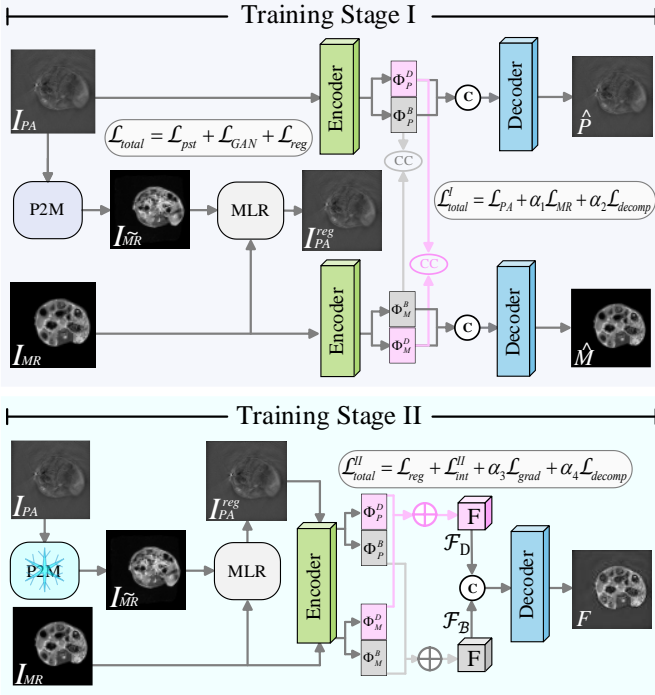


Fig. 5. Flowchart of the two-stage training strategy.

### 2.5.1. Training stage I

Firstly, for multimodal image registration, we transform the registration of multi-modal images into single-modal registration through the image synthesis network P2M, and jointly optimize the synthesis network and the registration network. Specifically, paired but unaligned PAT and MRI images \$\{I\_{PA}, I\_{MR}\}\$ are input into the synthesis network P2M to generate a pseudo MRI image \$I\_{MR}^{\sim}\$. The registration network MLR performs fine registration using the pseudo MRI and MRI images \$\{I\_{MR}^{\sim}, I\_{MR}\}\$ as inputs, generating multiscale affine parameters and performing spatial transformation on \$I\_{PA}\$. For the image fusion process in training stage I, we do not need well-registered PAT and MRI images. Specifically, unaligned PAT and MRI images \$\{P, M\}\$ are input into FE to extract shallow features \$\{\Phi\_P^S, \Phi\_M^S\}\$. Then, low-frequency basic features \$\{\Phi\_P^B, \Phi\_M^B\}\$ and high-frequency detail features \$\{\Phi\_P^D, \Phi\_M^D\}\$ of the two different modalities are extracted using BE and DE, respectively. Subsequently, the basic and detail features of PAT \$\{\Phi\_P^B, \Phi\_P^D\}\$ (or MRI

\$\{\Phi\_M^B, \Phi\_M^D\}\$) are concatenated and input into the decoder to reconstruct the original PAT image \$\hat{P}\$ (or MRI image \$\hat{M}\$).

### 2.5.2. Training stage II

We freeze the parameters of the well-trained image synthesis network P2M obtained in training stage I and jointly optimize the registration network and fusion network. Paired but unaligned PAT and MRI images \$\{I\_{PA}, I\_{MR}\}\$ are input into the image synthesis network trained in training stage I to obtain paired pseudo MRI and MRI images \$\{I\_{MR}^{\sim}, I\_{MR}\}\$. The pseudo MRI and MRI images are registered in the image registration network MLR, undergoing spatial transformation and correcting local misalignments, resulting in the registered PAT image \$I\_{PA}^{reg} = P\$. Then, the registered PAT and MRI images \$\{P, M\}\$ are input into the trained encoder to obtain decomposed features. The decomposed basic features \$\{\Phi\_P^B, \Phi\_M^B\}\$ and detail features \$\{\Phi\_P^D, \Phi\_M^D\}\$ are then input into the trained fusion layers \$F\_B\$ and \$F\_D\$, respectively. Finally, the fused features \$\{\Phi^B, \Phi^D\}\$ are input into the decoder to obtain the fused image \$F\$.

## 2.6. Loss functions

### 2.6.1. Perceptual style transfer loss

To generate more realistic pseudo MRI images, we introduce the perceptual style transfer (PST) loss to control the cycle consistency of P2M. The PST loss consists of two terms: the perceptual loss \$\mathcal{L}\_{pcp}\$ and the style loss \$\mathcal{L}\_{sty}\$. First, \$\mathcal{L}\_{pcp}\$ is defined as:

$$\mathcal{L}_{pcp}^{\psi_j} = \left\| \psi_j(I_{PA}) - \psi_j(G_B(G_A(I_{PA}))) \right\|^2 + \left\| \psi_j(I_{MR}) - \psi_j(G_A(G_B(I_{MR}))) \right\|^2 \quad (10)$$

where \$\psi\_j\$ is the \$j\$-th layer of the VGG-19 model (Simonyan and Zisserman, 2015), with \$j \in [2, 7, 12, 21, 30]\$, and corresponding weights \$\omega \in [\frac{1}{32}, \frac{1}{16}, \frac{1}{8}, 1, 1]\$. These features are also used to compute \$\mathcal{L}\_{sty}\$, which measures the statistical error between the pairs of images \$\{I\_{PA}^{\sim}, I\_{PA}\}\$ and \$\{I\_{MR}^{\sim}, I\_{MR}\}\$, and is defined as:

$$\mathcal{L}_{sty}^{\psi_j} = \omega_j \left\| \mathcal{G}_{\psi_j}(I_{PA}) - \mathcal{G}_{\psi_j}(G_B(G_A(I_{PA}))) \right\|^2 + \omega_j \left\| \mathcal{G}_{\psi_j}(I_{MR}) - \mathcal{G}_{\psi_j}(G_A(G_B(I_{MR}))) \right\|^2 \quad (11)$$

where \$\mathcal{G}\$ is the Gram matrix (Sajjadi et al., 2017), used to suppress checkerboard artifacts. The total PST loss is given by:

$$\mathcal{L}_{pst} = \lambda_p \mathcal{L}_{pcp} + \lambda_s \mathcal{L}_{sty} \quad (12)$$

where \$\lambda\_p\$ is set to 1, and \$\lambda\_s\$ is set to 100.

### 2.6.2. Registration loss

We employ bidirectional similarity loss to constrain the registration between MRI images and pseudo-MRI images, defined as:

$$\mathcal{L}_{sim}^{bi} = \left\| \psi_j(I_{MR}^{reg}) - \psi_j(I_{MR}^{\sim}) \right\| + \lambda_{rev} \left\| \psi_j(\phi^{\circ} I_{MR}^{\sim}) - \psi_j(I_{MR}) \right\|_1 \quad (13)$$

The first term corresponds to the forward deformation, while the second term corresponds to the backward deformation, with

a weight of  $\lambda_{rev} = 0.2$ . Here, the backward deformation field  $\phi$  is used to warp the pseudo-MRI image  $I_{MR}^{\sim}$ , making it close to the warped input  $I_{MR}$ . To ensure smooth deformation fields, we define the smoothness loss as:

$$\mathcal{L}_{smooth} = \|\nabla\phi\|_1 \quad (14)$$

Then, the overall registration loss is calculated by the following equation:

$$\mathcal{L}_{reg} = \mathcal{L}_{sim} + \lambda_{sm}\mathcal{L}_{smooth} \quad (15)$$

where  $\lambda_{sm}$  is set to 10 in our work.

In training stage I, we jointly train our synthesis and registration networks by minimizing the following overall loss function:

$$\mathcal{L}_{total} = \mathcal{L}_{pst} + \mathcal{L}_{GAN} + \mathcal{L}_{reg} \quad (16)$$

where  $\mathcal{L}_{GAN}$  inherits the functionality of CycleGAN (Zhu *et al.*, 2017) to discriminate between fake and real MRI images.

### 2.6.3. Fusion loss

In training stage I, the total loss  $\mathcal{L}_{total}^I$  of the image fusion network is calculated as:

$$\mathcal{L}_{total}^I = \mathcal{L}_{PA} + \alpha_1\mathcal{L}_{MR} + \alpha_2\mathcal{L}_{decomp} \quad (17)$$

where  $\mathcal{L}_{PA}$  and  $\mathcal{L}_{MR}$  denote the reconstruction losses of PAT and MRI images,  $\mathcal{L}_{decomp}$  represents the feature decomposition loss, and  $\alpha_1$  and  $\alpha_2$  are tuning parameters. The reconstruction loss ensures that the information contained in the images is preserved throughout the encoding and decoding processes.

$$\mathcal{L}_{PA} = \mathcal{L}_{int}^I(P, \hat{P}) + \mu\mathcal{L}_{SSIM}(P, \hat{P}) \quad (18)$$

The term  $\mathcal{L}_{int}^I(P, \hat{P}) = \|P - \hat{P}\|_2^2$  and  $\mathcal{L}_{SSIM}(P, \hat{P}) = 1 - SSIM(P, \hat{P})$ . Here,  $SSIM(\cdot, \cdot)$  represents the structural similarity index. Similarly,  $\mathcal{L}_{MR}$  can be obtained in the same manner. Additionally, the proposed feature decomposition loss  $\mathcal{L}_{decomp}$  is:

$$\mathcal{L}_{decomp} = \frac{(\mathcal{L}_{CC}^D)^2}{\mathcal{L}_{CC}^B} = \frac{(CC(\Phi_P^D, \Phi_M^D))^2}{(CC(\Phi_P^B, \Phi_M^B))} + \epsilon \quad (19)$$

where  $CC(\cdot, \cdot)$  denotes the correlation coefficient operator, and  $\epsilon$  is set to 1.01 to ensure that this term is always positive. The motivation behind this loss term is based on our assumption, where the decomposed features  $\{\Phi_P^B, \Phi_M^B\}$  are expected to contain more modality-shared information, hence they tend to be highly correlated. Conversely,  $\{\Phi_P^D, \Phi_M^D\}$  represent texture and detail information in  $P$  and soft tissue with clear edges in  $M$ , which are modality-specific. Therefore, the correlation of the feature mappings is lower. Empirically, under the guidance of gradient descent on  $\mathcal{L}_{decomp}$ ,  $\mathcal{L}_{CC}^D$  gradually approaches 0 while  $\mathcal{L}_{CC}^B$  increases, aligning with our intuition about feature decomposition.

Subsequently, in training stage II, we freeze the image synthesis network and jointly optimize the registration and fusion networks. The total loss is given by:

$$\mathcal{L}_{total}^{II} = \mathcal{L}_{reg} + \mathcal{L}_{int}^{II} + \alpha_3\mathcal{L}_{grad} + \alpha_4\mathcal{L}_{decomp} \quad (20)$$

where  $\mathcal{L}_{int}^{II} = \frac{1}{HW} \|I_f - \max(I_{PA}, I_{MR})\|_1$  and  $\mathcal{L}_{grad} = \frac{1}{HW} \|\|\nabla I_f\| - \max(\|\nabla I_{PA}\|, \|\nabla I_{MR}\|)\|_1$ . Here,  $\nabla$  represents the Sobel gradient operator.  $\alpha_3$  and  $\alpha_4$  are tuning parameters.

## 3. Experimental setup

### 3.1. Data acquisition

For PAT imaging, a commercial small animal multispectral optoacoustic tomography system (MSOT inVision128, iThera Medical, Germany) is used. The system features tunable (660-960 nm) lasers with a pulse width of about 5 ns and a repetition rate of 10 Hz. Ultrasonic waves generated by stimulated samples are coupled through water and transmitted to a ring array transducer consisting of 128 elements. All MRI scans are performed on a 7T small animal MRI system (Pharmascan, Bruker, Germany), as detailed in Zhang *et al.* (Zhang *et al.*, 2022). Furthermore, during data acquisition, we utilize a dual-modal animal imaging bed previously reported by our group (Zhang *et al.*, 2021b), which effectively immobilizes animal posture and position during modal switching.

### 3.2. Animal experiment

All animal experiments have received approval from the local animal ethics committee of southern medical university and are conducted according to current guidelines. In vivo animal imaging experiments involve six healthy female nude mice (12-15 g each, Southern Medical University, Guangzhou, China) and four 4T1 breast cancer nude mice (Southern Medical University Cancer Institute, Guangzhou, China).

### 3.3. Implementation details

The algorithm <sup>1</sup> is implemented in Python, utilizing the PyTorch framework. It runs on an Ubuntu system with Intel Xeon E5-2667 CPU (3.2 GHz) and NVIDIA TITAN X Pascal GPU. During preprocessing, images are resized to 300×300 pixels. Data augmentation techniques including rotation and flipping result in a final dataset of 2384 pairs of PAT-MRI training data. Training is conducted for 120 epochs, with 40 epochs in the first stage and 80 epochs in the second stage. The Adam optimizer is used for model optimization with an initial learning rate of  $10^{-3}$ , reduced by a factor of 0.5 every 20 epochs. Network hyperparameters include 4 Restormer blocks with 8 attention heads and 64 dimensions in the FE, while the BE contains LT blocks with the same dimensions and attention heads. The decoder configuration mirrors that of the encoder. For the loss functions in Eq. (17) and (20),  $\alpha_1$  to  $\alpha_4$  are set to 1, 2, 10, and 2 respectively, ensuring consistent magnitudes for each term.

<sup>1</sup><https://github.com/zhongniuniu/PAMRFuse-plus>

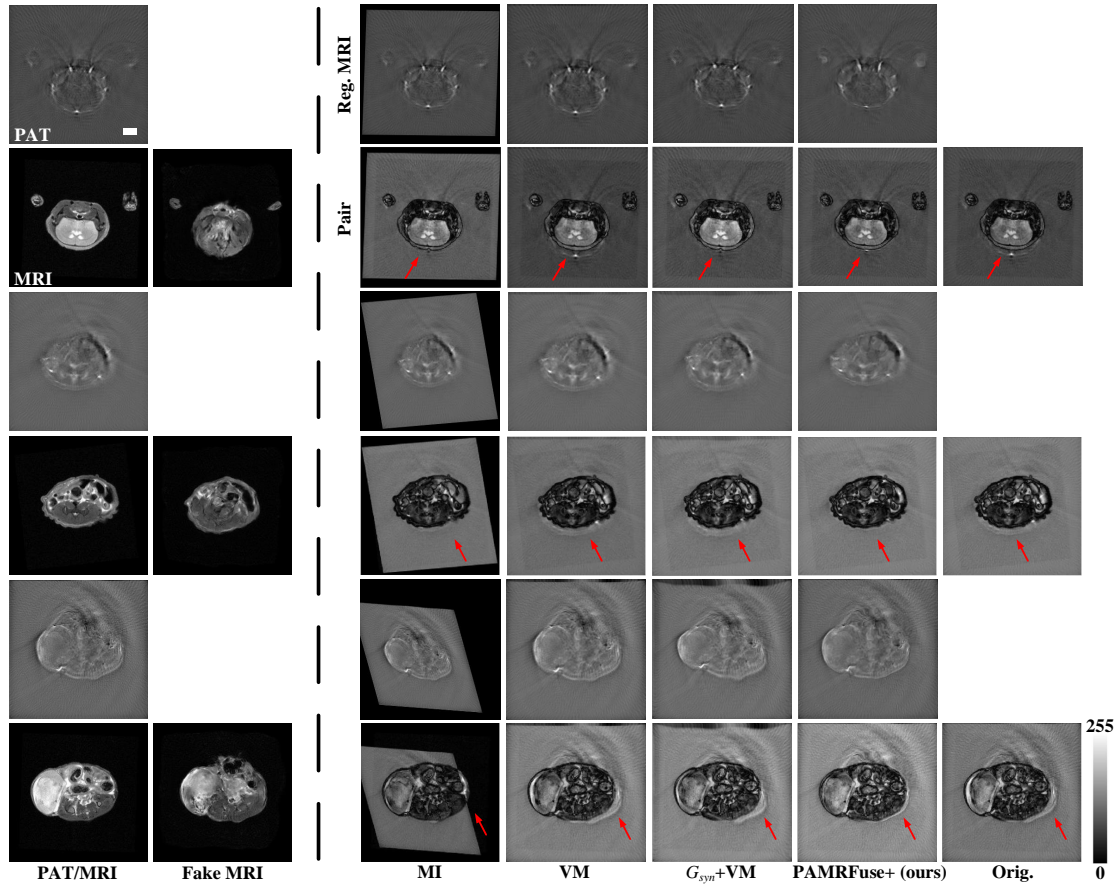


Fig. 6. Synthesis and registration results of unaligned PAI-MRI image pairs. Reg. MRI: MRI image after image registration. Orig.: Unaligned MRI overlaid on PAT. Under the registration results, the distorted MRI images are shown in pairs with the PAI images to demonstrate their misalignment. Scale bar, 3mm.

## 4. Experimental results

### 4.1. PAT-MRI image synthesis and registration

Given the scarcity of multi-modal image alignment methods, we compare PMNet with classical multi-modal registration methods, including mutual information (MI) (Viola and Wells, 1995) and Voxelmorph (VM) (Balakrishnan et al., 2019). Both MI and VM are capable of handling non-rigid deformations when estimating deformation fields.

#### 4.1.1. Qualitative analysis

The synthesis and registration results of PAT and MRI are shown in Fig.6. In each group, the deformed PAT images and the reference MRI source images are overlaid to display misalignment. Despite the use of dual-modal animal imaging bed (Zhang et al., 2021b) for acquiring original PAT and MRI data, significant distortion at the edges or misalignment with corresponding anatomical structures cannot be entirely avoided, as shown in the last column of Fig.6. Due to the significant modality differences between medical modalities, limited structural information in PAT images, and high degrees of non-rigid transformation, it is challenging to generate accurate inverse deformation fields. MI can successfully handle some PAT-MRI misalignment scenarios and correct partial deformations, as shown in the first group of Fig.6, but severe geometric distortions are

prevalent in most image pairs, as readily observed in the last group of Fig.6. While PAT after the original VM registration does not exhibit severe geometric distortions, it fails to align PAT-MRI images and may even exacerbate deformations. Our PAMRFuse+ method, before registration, utilizes the image synthesis network P2M to synthesize pseudo MRI images from PAT, simplifying multimodal PAT-MRI image registration compared to single-modal MRI image registration. Example synthesis results as shown in the second column of Fig.6, demonstrate that the structure depicted in the synthesized MRI images is largely consistent with real MRI images (synthesized MRI images are unaligned with real MRI images), accurately representing anatomical structures crucial for subsequent image registration tasks. More importantly, pseudo-MRI images eliminate the influence of severe scattering artifacts in the PAT image background on the registration process. The effectiveness of our registration method is evident from the clear improvement in the regions indicated by the red arrows in Fig.6. These results indicate that our approach outperforms the comparison methods, offering higher registration accuracy.

#### 4.1.2. Quantitative results

We used three commonly used metrics to evaluate the registration results, including mutual information (MI) (Qu et al., 2002), normalized mutual information (NMI), and normalized



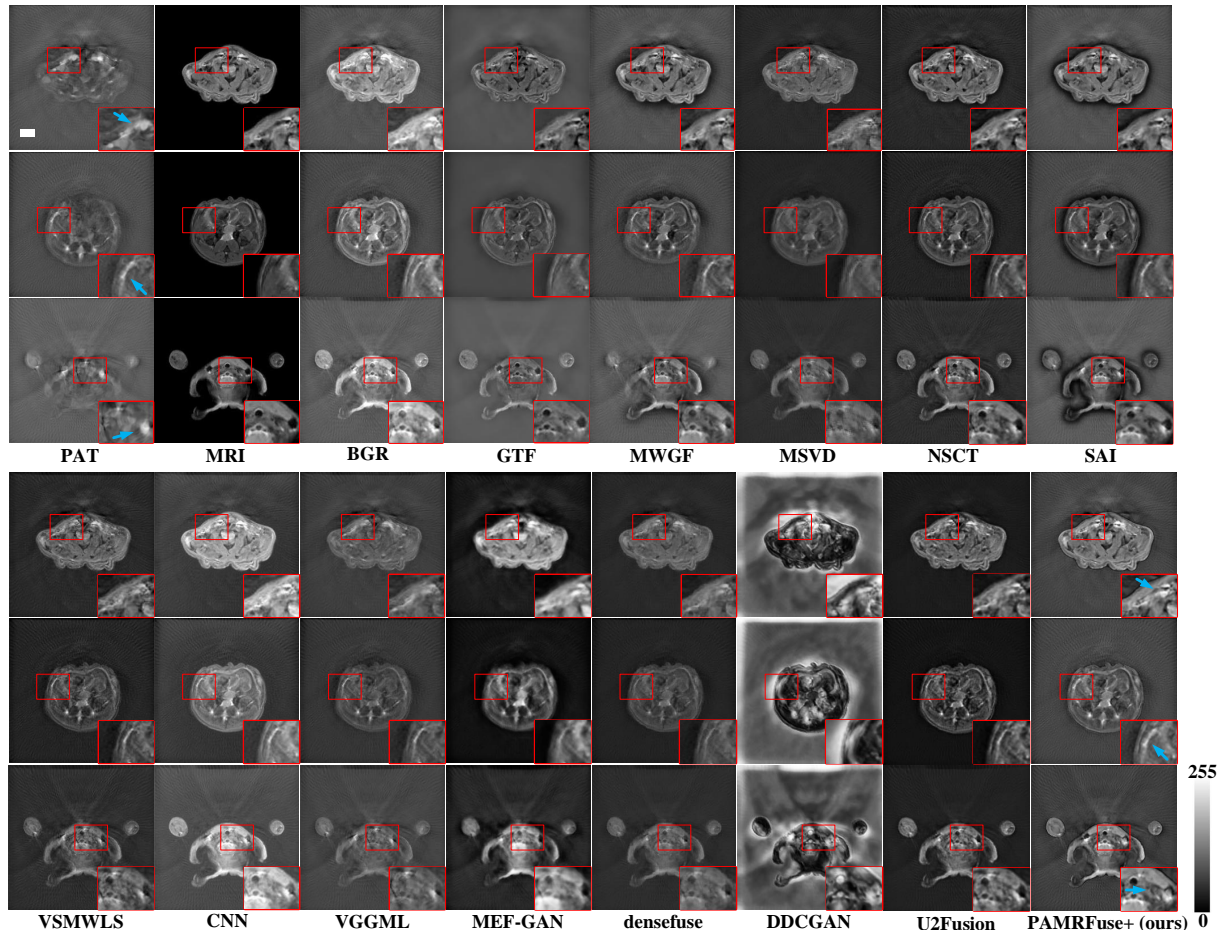


Fig. 7. Fusion results of unaligned PAT-MRI image pairs. The red boxes are enlarged to provide a clearer comparison of the differences among the results of various methods. The blue arrows indicate the region of high-intensity brightness information from PAT. PAMRFuse+ effectively eliminates misalignment while retaining the soft tissue details of the original MRI images, and the brightness information of the original images is successfully preserved. Scale bar, 3mm.

cross-correlation (NCC) (Han et al., 2013b), as shown in Table 1. The improvement generated by the MI algorithm in performing cross-modal alignment of PAT-MRI images can be negligible, with the CC metric even performing worse than the unaligned input. Meanwhile, the results of direct registration using the VM algorithm show that all metrics are worse compared to the unaligned input. In contrast, our PAMRFuse+ achieves improvements in all three metrics compared to the unaligned input and achieves the best performance. Specifically, the proposed cross-modal generation and registration method achieve approximately 9.79%, 9.47%, and 38.35% improvements in the MI, NMI, and CC metrics, respectively. These findings demonstrate that the proposed PAMRFuse+ is more effective than existing multimodal image alignment methods.

Table 1. Quantitative comparison of registration accuracy (mean, red: best).

Methods	MI $\uparrow$	NMI $\uparrow$	CC $\uparrow$
Misaligned Input	0.2807	0.1119	0.2096
MI	0.3016	0.1194	0.1947
VM	0.2696	0.1071	0.1904
P2M+VM	0.2923 <sup>10.0227</sup>	0.1154 <sup>10.0083</sup>	0.2176 <sup>10.0272</sup>
<b>PAMRFuse+ (ours)</b>	<b>0.3082</b>	<b>0.1225</b>	<b>0.2900</b>

## 4.2. PAT-MRI image fusion

We compared PAMRFuse+ with state-of-the-art (SOTA) fusion methods, including BGR (Zhang et al., 2017), GTF (Ma et al., 2016), MWGF (Zhou et al., 2014), MSVD (Naidu, 2011), NSCT (Yang et al., 2007), SAI (Li et al., 2018b), VSMWLS (Ma et al., 2017), CNN (Liu et al., 2018), VGGML (Li et al., 2018a), MEF-GAN (Xu et al., 2020), densefuse (Li and Wu, 2019), DDCGAN (Ma et al., 2020), and U2Fusion (Xu et al., 2022). BGR, GTF, MWGF, MSVD, NSCT, SAI, and VSMWLS are traditional image fusion methods. CNN, VGGML, densefuse, and U2Fusion are end-to-end image fusion methods, while MEF-GAN and DDCGAN are GAN-based image fusion methods.

### 4.2.1. Qualitative analysis

Since SOTA fusion methods cannot handle unaligned data, for fair comparison, the registration method P2M+VM ranked second in Section 4.1, is used as their pre-registration operation. In other words, PAMRFuse+ is compared with the combination of P2M+VM and SOTA fusion methods to assess fusion performance and observe the importance of registration for image fusion. Qualitative results are shown in Fig.7. In the third

**Table 2. Quantitative comparison of fusion performance (mean, red: best).**

	MI↑	VIF↑	Qabf↑	SF↑	SSIM↑	FMI <sub>pixel</sub> ↑	FMI <sub>dct</sub> ↑	FMI <sub>w</sub> ↑
<b>Aligned Method: P2M + Voxelmorph</b>								
BGR	2.8405	0.7860	0.5202	0.0402	0.9284	0.8917	0.2080	0.2031
GTF	1.7997	0.5441	0.3401	0.0301	0.8478	0.8904	0.2317	0.1493
MWGF	2.0958	0.7941	0.5440	0.0390	0.9048	0.9025	0.2127	0.1975
MSVD	2.4940	0.6187	0.2753	0.0283	0.8884	0.8822	0.1896	0.1668
NSCT	2.2099	0.6541	0.5004	0.0395	0.9407	0.8987	0.2156	0.1983
SAI	2.2028	0.7558	0.5456	0.0384	0.8946	0.8996	0.2065	0.1975
VSMWLS	2.3324	0.7026	0.4307	0.0354	0.9256	0.8828	0.2051	0.1980
CNN	2.1382	0.8323	0.5446	0.0393	0.9421	0.8980	0.2073	0.1996
VGGML	2.5039	0.6983	0.3635	0.0250	0.8946	0.8910	0.1861	0.1838
MEF-GAN	2.7033	0.7265	0.3325	0.0289	0.9078	0.8829	0.1908	0.2433
densefuse	3.1141	0.6148	0.3345	0.0237	0.9273	0.8875	0.2881	0.2922
DDCGAN	1.6878	0.0417	0.2661	0.0418	0.3866	0.8629	0.2248	0.1671
U2Fusion	3.0122	0.6378	0.4319	0.0375	0.9549	0.8875	0.2981	0.2925
<b>PAMRFuse+ (ours)</b>	<b>4.2421</b>	<b>0.8421</b>	<b>0.7099</b>	<b>0.0434</b>	<b>0.9629</b>	<b>0.9077</b>	<b>0.3040</b>	<b>0.4498</b>

set of PAT-MRI images in Fig.7, significant non-rigid misalignments are present in the source images. By observing locally magnified regions, we can see that misalignments still exist in the competitors' results, resulting in overlapping shadows and blurred textures. In contrast, the proposed method demonstrates good alignment and fusion capabilities. While preserving clear structures and adjusting the misalignment to provide a clearer description of the scene. In the first and second sets of PAT-MRI image pairs in Fig.7, the source images are almost aligned, so we focus on comparing fusion performance. In the competitors, there are noticeable color distortions in BGR, CNN, MEF-GAN, and DDCGAN. MSVD and U2Fusion methods can extract sufficient spatial details from the source images, but the fused images produce adverse artifacts not present in the source images, which somewhat diminishes visual perception. NSCT, VSMWLS, and MEF-GAN methods effectively prevent visual artifacts but are prone to losing energy contained in the source images, leading to decreased brightness and contrast in certain areas of the fused images. The main drawbacks of MWGF and VGGML methods lie in their limited ability to preserve details, with many small details from the source images observed to be blurred in the fused images. GTF and densefuse overly preserve the texture of MRI images, weakening the functional information in PAT images. Compared to the above methods, PAMRFuse+ performs well in preserving both the texture structure information in MRI images and the functional information in PAT images, resulting in richer and clearer texture details and stronger tissue contrast.

#### 4.2.2. Quantitative results

Table 2 presents a quantitative comparison of the fusion results of PAT-MRI. Compared to the other 13 methods, our approach significantly outperforms existing fusion methods, ranking first in all eight metrics including MI, VIF (Han et al., 2013a), Qabf (Xydeas and Petrovic, 2000), SF (Eskicioglu and Fisher, 1995), SSIM, FMI<sub>pixel</sub>, FMI<sub>dct</sub>, and FMI<sub>w</sub> (Haghighat et al., 2011). These results demonstrate that our method preserves more image feature information and generates higher-quality and clearer fusion images. Specifically, the optimal MI, SSIM, and FMI imply that the corresponding fusion algorithms transfer more information from the source images to the

fused images, where FMI<sub>pixel</sub>, FMI<sub>dct</sub>, and FMI<sub>w</sub> respectively compute the mutual information of pixel, discrete cosine, and wavelet features. The optimal VIF and Qabf indicate that our fusion images exhibit minimal distortion while achieving better visual perception, aligning more closely with human visual perception. A higher SF suggests richer edge and texture details.

#### 4.3. Task-driven evaluation

The fused medical images not only enhance the quality of visual observation but also serve as a crucial aid for advanced visual tasks. However, existing evaluation methods only focus on the visual quality and statistical metrics of medical fusion images. In this section, we break away from the constraints of existing medical image fusion quality assessment methods and propose a task-driven evaluation criterion. Specifically, we perform body contour segmentation and multi-organ instance segmentation tasks on the PAT-MRI fused images, and observe and compute segmentation performance using specific metrics under different fusion methods.

##### 4.3.1. Contour segmentation results

To ensure a fair comparison, we train separate segmentation networks for different fusion algorithms. The segmentation network uses a recently proposed small-animal PAT image contour automatic segmentation method based on an optimal graph search algorithm (Liang et al., 2022). Initially, fusion images are generated using each fusion method. Subsequently, 14 segmentation models are trained and tested individually on the PAT, MRI, and 14 fusion image datasets. Visual examples are provided in Fig.8. From the results, it is observed that most fusion algorithms can integrate complementary information from source images to some extent, achieving a more comprehensive description of the imaging scene. Consequently, the segmentation model can achieve satisfactory segmentation results on fusion images in most cases. However, severe dark patches exist in the fusion results of the MWGF, SAI, and DDCGAN methods, undermining the complementary information from source images and resulting in disappointing segmentation outcomes. Additionally, misalignment in fusion results also adversely affects contour segmentation. In the third group of PAT-MRI image pairs, misalignment at contour boundaries leads to overlap-

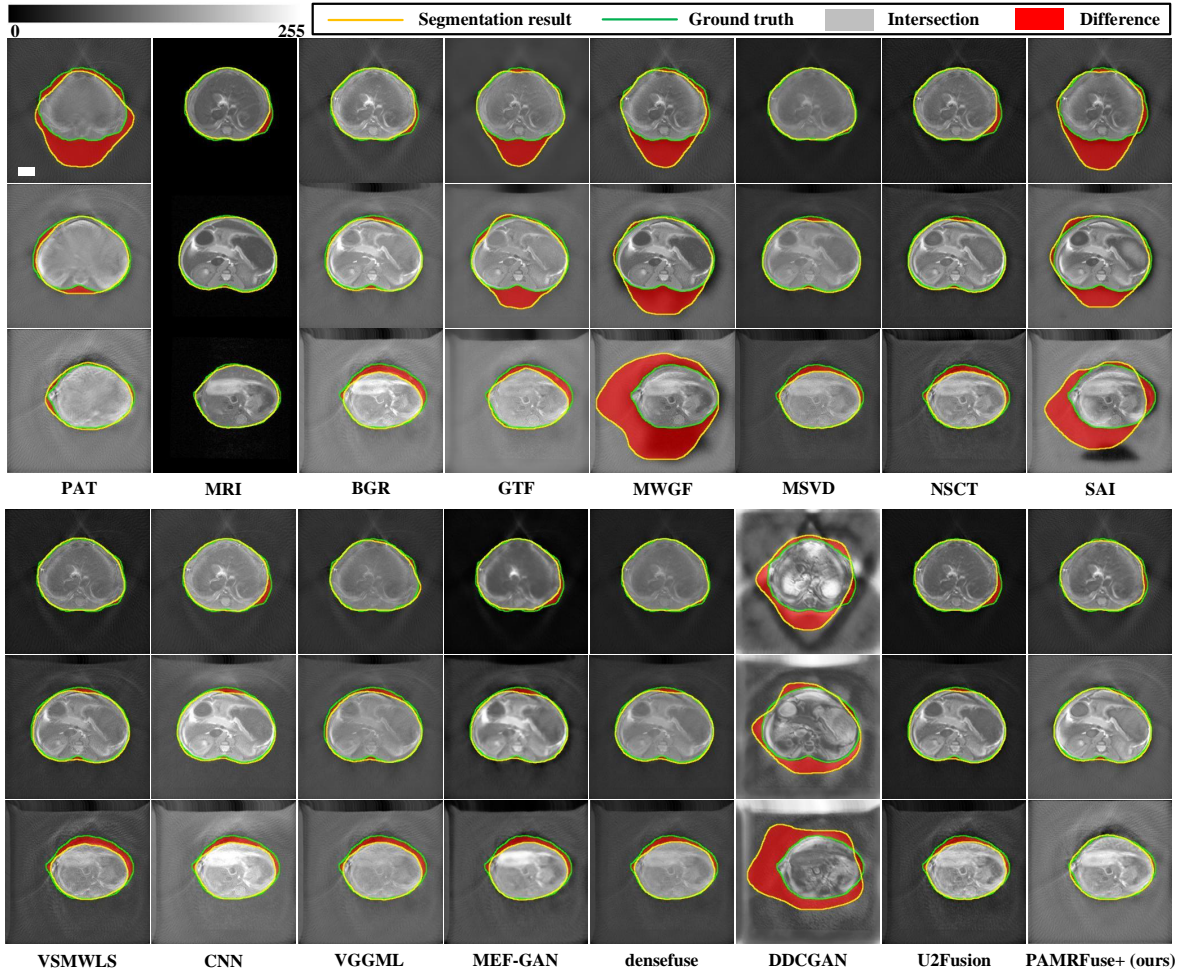


**Fig. 8.** Results of contour segmentation. The non-overlapping of the automatic algorithmic and manual method segmentation masks is indicated in red, and their intersection is indicated in white. The yellow line is the algorithmic segmented contour and the green line is the manually segmented contour. scale bar, 3mm.

ping in the fusion images of the comparative methods, resulting in varying degrees of errors in boundary segmentation results. Conversely, when image registration is well-performed, fusion information from both modalities positively influences segmentation results, as evident in the segmentation results of our method. Furthermore, in the first and second groups of PAT-MRI image pairs, image misalignment is tiny. In such cases, most fusion methods enhance the accuracy of contour segmentation compared to PAT images and our fused images yielding the best segmentation results. Table 3 reports the quantitative results. It can be observed that our algorithm ranks first in dice coefficient (DSC), hausdorff distance (Haus), intersection-over-union (IoU), and mean surface distance (MSD) metrics. We attribute this superiority to two factors. Firstly, the proposed cross-modal generation registration paradigm effectively eliminates misalignment between PAT and MRI, alleviating the occurrence of overlap in fusion results. Secondly, our fusion network fully integrates complementary information from PAT and MRI images. This complementary information aids the segmentation model in comprehensively understanding imaging scenes, which is a key reason why fusion can enhance segmentation performance.

#### 4.3.2. Multi-organ instance segmentation results

As a fundamental task in computer vision, instance segmentation performance effectively reflects the semantic information in fused images. Therefore, we employ a SOTA PAT instance segmentation model, the structure fusion enhanced graph convolutional multi-organ instance segmentation pipeline (SFE-GCN), to evaluate multi-organ instance segmentation performance on fused images. 14 instance segmentation models are trained separately on the PAT, MRI, and 14 fusion image training datasets. We randomly select 45 images from the PAT-MRI dataset as the test dataset, covering nearly all anatomical sites. Eight key organ categories are manually annotated in these images. Visual examples in Fig.9 illustrate the advantages of fusion algorithm in facilitating multi-organ instance segmentation. In PAT imaging scenes, organs such as kidneys, spine, spleen, heart, tumors, and lungs cannot be segmented due to imaging depth limitations. However, the spleen cannot be segmented in MRI imaging scenes. After enhancement by various fusion methods, segmentation of some organs is improved. For instance, in the first image pair, BGR, SAI, and PAMRFuse+ successfully segment the spleen. However, inappropriate fusion may weaken significant targets due to interference from

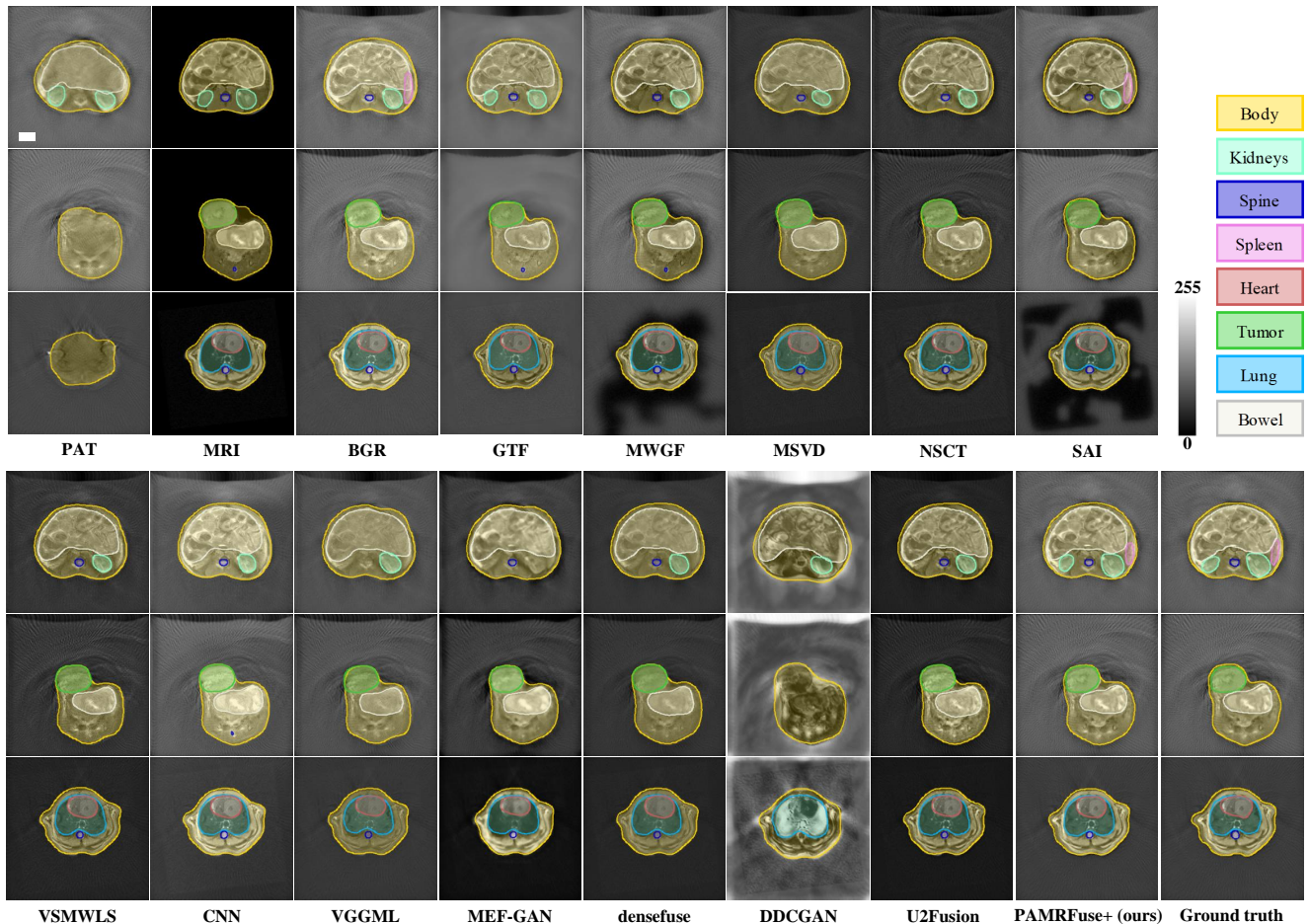


Fig. 9. Results of multi-organ segmentation. Segmentations produced by each fusion method are shown as filled translucent regions. scale bar, 3mm.

Table 3. Quantitative evaluation of the contour segmentation accuracy (mean, red: best).

Method	DSC $\uparrow$	Haus $\downarrow$	IoU $\uparrow$	MSD $\downarrow$
PAT	69.114	5.440	0.535	2.128
MRI	76.713	3.360	0.623	1.533
BGR	76.603	3.328	0.617	1.533
GTF	71.106	4.937	0.556	1.993
MWGF	70.891	5.281	0.553	2.046
MSVD	76.330	3.327	0.618	1.554
NSCT	76.628	3.239	0.621	1.533
SAI	70.180	5.485	0.545	2.105
VSMWLS	76.486	3.234	0.620	1.537
CNN	76.276	3.328	0.617	1.557
VGGML	76.432	3.188	0.619	1.534
MEF-GAN	76.457	3.195	0.619	1.531
densfuse	76.305	3.334	0.617	1.556
DDCGAN	70.605	4.727	0.547	2.089
U2Fusion	76.736	3.234	0.623	1.523
<b>PAMRFuse+ (ours)</b>	<b>77.007</b>	<b>3.140</b>	<b>0.626</b>	<b>1.502</b>

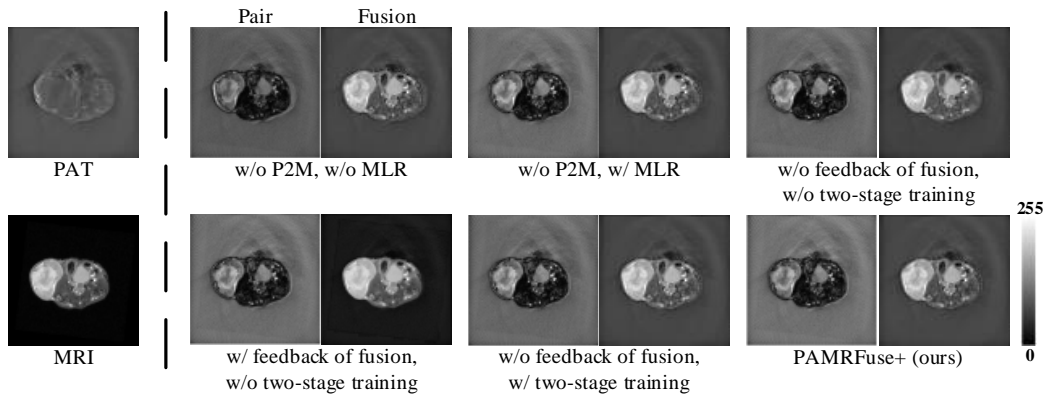
negative and irrelevant information. For instance, in the first image pair, the left kidney could have been segmented in PAT and MRI source images, gets unsegmented after enhancement by most contrast fusion methods. Additionally, erroneous or insufficient fusion may weaken complementary information from source images, leading to incorrect organ segmentation. For

example, in the second image pair, GTF, MWGF, and CNN erroneously segment a non-existent spine. In contrast, our fused images with high contrast, rich textures, and prominent targets, contribute to effective organ segmentation. Therefore, SFE-GCN successfully segments all target organs from our fused images, proving that our fusion images provide more semantic information for downstream tasks.

We further employ quantitative metrics to assess multi-organ instance segmentation tasks. Using DSC metric to measure segmentation performance, results are presented in Table 4. MRI images achieve the highest DSC values for the spine, indicating that MRI images provide sufficient semantic information about the spine for the segmentation network. However, the segmentation results for the spleen and tumors in MRI images are disappointing. Fortunately, PAT images can provide rich semantic information about the spleen and tumors for the segmentation network. In PAT imaging scenes, the spleen and tumors exhibit rich vascular structures, with signal values typically higher than surrounding tissues. An ideal fusion algorithm can integrate complementary information from PAT and MRI images, yielding fusion images with satisfactory organ segmentation performance. In Table 4, our fusion results show the highest DSC values for most organs. These findings demonstrate that PAMRFuse+ effectively integrates the photoacoustic signals from PAT images and the soft tissue information from MRI images,

**Table 4. Quantitative evaluation of the multi-organ instance segmentation accuracy (mean, red: best).**

Method	Body	Brain	Lung	Heart	Intestines	Kidneys	Spleen	Spine	Tumor
PAT	66.96	/	/	/	30.66	13.75	/	/	/
MRI	95.85	95.25	95.97	93.11	93.91	79.85	36.53	<b>82.96</b>	54.57
BGR	95.28	93.95	96.48	84.14	92.23	72.75	34.30	70.51	60.09
GTF	95.11	88.62	96.42	91.86	87.97	77.23	46.06	76.83	52.68
MWGF	88.74	95.14	96.19	93.56	89.54	77.12	35.16	77.39	71.64
MSVD	92.47	90.72	95.85	90.83	87.23	61.57	/	74.17	68.80
NSCT	95.98	93.75	96.21	90.28	92.55	72.84	18.33	73.90	69.55
SAI	94.02	94.51	96.36	89.59	92.67	76.48	25.42	73.25	69.38
VSMWLS	90.83	91.97	96.27	87.09	89.70	60.10	/	71.48	59.86
CNN	96.25	94.56	95.97	91.11	88.92	72.90	26.86	75.31	87.44
VGGML	91.99	81.00	95.93	69.98	81.93	38.14	9.10	48.09	42.07
MEF-GAN	93.98	91.40	95.44	82.22	91.57	43.03	9.78	68.54	82.06
densefuse	95.86	93.34	96.72	91.14	88.51	73.26	18.01	77.19	77.96
DDCGAN	86.80	48.43	52.43	/	73.16	4.15	/	7.02	7.40
U2Fusion	95.46	91.41	<b>96.89</b>	88.95	92.35	72.50	8.34	77.56	61.11
<b>PAMRFuse+ (ours)</b>	<b>98.04</b>	<b>95.54</b>	96.12	<b>93.60</b>	<b>94.49</b>	<b>88.86</b>	<b>84.08</b>	80.77	<b>88.25</b>

**Fig. 10. Visualized results of ablation studies.**

resulting in enhanced organ recognition and segmentation, thus achieving the highest segmentation accuracy in multi-organ instance segmentation tasks.

#### 4.4. Ablation study

##### 4.4.1. Validity of synthetic and alignment networks

Two key components of our fusion framework are the synthesis network P2M and the registration network MLR, which effectively collaborate to mitigate the misalignment between PAT and MRI, reducing artifacts during the fusion process. To evaluate their effectiveness, we conducted ablation experiments on P2M and MLR. In Section 4.1, we inserted the image synthesis network P2M into VM as an enhanced version. As shown in Table 5, the quantitative results obtained with P2M in conjunction with VM showed improvements over the original version across all metrics, with MI, NMI, and CC metrics achieving approximately 8.41%, 7.41%, and 14.28% improvements, respectively. Additionally, visual comparisons provided in Fig.10 demonstrate the enhanced accuracy of the registration results generated by the VM model equipped with P2M, further confirming the efficacy of P2M.

In this subsection, we comprehensively validate the effectiveness of P2M and MLR from both the perspective of image reg-

istration and fusion. As illustrated in Fig.10, the direct fusion of unaligned images using DFDF (w/o P2M, w/o MLR) results in noticeable artifacts. Firstly, assuming the absence of P2M, we investigate the impact of the registration network MLR on the unaligned PAT-MRI fusion task. Compared to directly fusing unaligned PAT-MRI images, the utilization of MLR alleviates misalignment in the images, contributing to producing fusion results with negligible artifacts. Moreover, quantitative results in Table 5 demonstrate improvements across most fusion metrics. To further enhance the accuracy of PAT-MRI image registration, we introduce the P2M network, simplifying the multimodal PAT-MRI registration into a single-modal MRI registration. As reported in Table 5 and demonstrated qualitatively in Fig.10, the combined use of P2M and MLR significantly enhances the performance of both registration and fusion in multimodal registration.

##### 4.4.2. Training strategy comparison

To comprehensively enhance the performance of registration and fusion, we propose a joint adaptive two-stage training strategy. Specifically, besides employing the synthetic-registration and registration-fusion joint training strategies, we adopt a two-stage training approach for the fusion network. The effective-

Table 5. Quantitative results of ablation studies. (mean, red: best).

(P2M, MLR)	Registration metrics			Metrics							
	MI	NMI	CC	MI	VIF	Qabf	SF	SSIM	FMI <sub>pixel</sub>	FMI <sub>det</sub>	FMI <sub>w</sub>
( <del>X</del> , <del>X</del> )	\	\	\	1.5281	0.4590	0.3958	0.0438	0.7240	0.8927	0.2071	0.1500
( <del>X</del> , ✓)	0.3019	0.1199	0.2826	1.5532	0.4672	0.3956	0.0428	0.7309	0.8941	0.2134	0.1515
(✓, ✓)	<b>0.3082</b>	<b>0.1225</b>	<b>0.2900</b>	<b>4.2421</b>	<b>0.8421</b>	<b>0.7099</b>	<b>0.0434</b>	<b>0.9629</b>	<b>0.9077</b>	<b>0.3040</b>	<b>0.4498</b>
<b>(feedback of fusion, two-stage training)</b>											
( <del>X</del> , <del>X</del> )	0.3026	0.1203	0.2796	1.4794	0.4075	0.3189	0.0377	0.7116	0.8829	0.1807	0.1438
(✓, <del>X</del> )	0.3033	0.1205	0.2813	1.6235	0.4652	0.3225	0.0372	0.7523	0.8897	0.2349	0.1638
( <del>X</del> , ✓)	0.3026	0.1203	0.2796	1.5504	0.4653	0.3953	0.0427	0.7303	0.8940	0.2133	0.1513
(✓, ✓)	<b>0.3082</b>	<b>0.1225</b>	<b>0.2900</b>	<b>4.2421</b>	<b>0.8421</b>	<b>0.7099</b>	<b>0.0434</b>	<b>0.9629</b>	<b>0.9077</b>	<b>0.3040</b>	<b>0.4498</b>

ness of the synthetic-registration joint training strategy has been validated in Section 4.4.1. In this section, we conduct comparative experiments to validate the effectiveness of registration-fusion joint training strategy and the two-stage training strategy for the fusion network. The registration and fusion results are depicted in Fig.10, where "w/ feedback of fusion" denotes the joint optimization of the registration and fusion networks, and "w/ two-stage training" indicates the adoption of the two-stage training strategy for the fusion network. If we abandon the joint optimization of the registration and fusion networks and discard the two-stage training, i.e., directly training the encoder, decoder, and fusion layer simultaneously, it can be observed that most registration and fusion metrics in Table 5 yield the least desirable performance. When we introduce the registration-fusion joint training strategy alone leads to improvements in most registration and fusion metrics, implying enhancements in registration performance and fusion image quality. However, even with the adoption of the registration-fusion joint training strategy, the fusion results as shown in Fig.10 are still suboptimal, with a noticeable decrease in tissue contrast. Upon solely employing the two-stage training strategy, the overall image contrast approaches that of our PAMRFuse+ results. Moreover, the degree of improvement in fusion metrics in Table 5 is greater than when solely introducing the registration-fusion joint optimization strategy, indicating the criticality of this strategy for training the fusion network. These results demonstrate that two-stage training can effectively alleviate training difficulties and enhance robustness. Finally, when combining the registration-fusion joint training strategy with the two-stage training strategy for the fusion network, superior registration accuracy and fusion quality are observed in both qualitative comparisons and metric evaluations. In summary, the ablation results above confirm the effectiveness and rationality of our network design, explaining the superiority of our overall framework which relies on the cooperation of each component.

## 5. Discussion

The purpose of our image fusion is to synthesize a fused image that not only contains prominent targets and rich texture details but also facilitates the completion of advanced visual tasks. Current medical image fusion algorithms face

some pressing challenges, including source image misalignment, pre-registration operation requirement, insufficient cross-model feature extraction, and the lack of validation on advanced visual tasks.

The proposed PAMRFuse+ addresses the limitations of existing multi-modal image registration and fusion methods, and achieves them in a mutually reinforcing framework. Specifically, the proposed style transfer network P2M addresses the misalignment issue between image pairs of different modalities and the challenges of multi-modal registration, and the multi-level fine registration network MLR performs image registration in a single-modal environment. In PAT-MRI image synthesis and registration experiments, excellent performance is observed in registering unaligned multi-modal images.

Secondly, the dual-branch feature decomposition fusion network DFDF tackles the problem of insufficient cross-modal feature extraction in current CNN-based image fusion networks. The quantitative and qualitative results of fusion experiments demonstrate that our fusion network DFDF can efficiently extract mode-specific features and shared features, and decompose them intuitively through the decomposition loss. Thirdly, in order to maintain the performance balance among the multi-task models, we have specially designed a two-stage training learning scheme. In order to validate the effectiveness of our proposed method, we conducted relevant ablation experiments, i.e., exploring the effects of synthesis and alignment networks, alignment and fusion mutual enhancement strategies, and two-step fine-training strategies on the fusion effect, respectively.

Finally, we conducted task-driven evaluation experiments to demonstrate the impact of image fusion on advanced visual tasks. The performance comparison of various fusion algorithms in body contouring and multi-organ segmentation results reveals the advantages of our framework in promoting advanced visual tasks. To our knowledge, this is the first time that advanced medical image visual tasks have been used to evaluate the effectiveness of image fusion.

## 6. Conclusion

In this paper, we propose an unsupervised PAT and MRI image fusion model for facilitating advanced visual tasks, named PAMRFuse+. Firstly, we simplify the alignment of cross-modal image pairs into single-modal registration using a generation

registration paradigm. Secondly, we introduce a multi-level fine registration network to predict the displacement vector field and perform registration reconstruction. Thirdly, a dual-branch feature decomposition fusion network is developed to effectively extract unique features and shared features from each modality. Extensive experimental results demonstrate the outstanding capability of PAMRFuse+ in fusing unaligned PAT-MRI images. Importantly, task-driven evaluation experiments including contour segmentation and multi-organ semantic segmentation reveal the inherent advantages of our approach in promoting high-level visual tasks.

## Declaration of Competing Interest

The authors declare that they have no known competing financial interests or personal relationships that could have appeared to influence the work reported in this paper.

## CRedit authorship contribution statement

**Yutian Zhong:** Methodology, Software, Validation, Formal analysis, Investigation, Data curation, Writing – original draft, Writing – review & editing, Visualization. **Jinchuan He:** Methodology, Software, Investigation, Resources. **Zhichao Liang:** Data curation, Investigation, Resources. **Shuangyang Zhang:** Data curation, Resources. **Qianjin Feng:** Resources. **Wufan Chen:** Project administration. **Li Qi:** Conceptualization, Methodology, Validation, Formal analysis, Resources, Writing – original draft, Writing – review & editing, Supervision, Project administration, Funding acquisition.

## Acknowledgments

This work was supported in part by National Natural Science Foundation of China (62371220), Guangdong Basic and Applied Basic Research Foundation (2021A1515012542, 2022A1515011748), and Guangdong Pearl River Talented Young Scholar Program (2017GC010282).

## References

Balakrishnan, G., Zhao, A., Sabuncu, M.R., Guttag, J., Dalca, A.V., 2019. Voxelmorph: A learning framework for deformable medical image registration. *IEEE Transactions on Medical Imaging* 38, 1788–1800. doi:10.1109/tmi.2019.2897538.

Chen, Z., Gezginer, I., Augath, M.A., Ren, W., Liu, Y.H., Ni, R., Deán-Ben, X.L., Razansky, D., 2022. Hybrid magnetic resonance and optoacoustic tomography (mrot) for preclinical neuroimaging. *Light-Science and Applications* 11. doi:10.1038/s41377-022-01026-w.

Cvejic, N., Bull, D., Canagarajah, N., 2007. Region-based multimodal image fusion using ica bases. *IEEE Sensors Journal* 7, 743–751. doi:10.1109/jsen.2007.894926.

Dinh, L., Sohl-Dickstein, J., Bengio, S., 2017. Density estimation using real nvp. *International Conference on Learning Representations (ICLR)* URL: <https://arxiv.org/abs/1605.08803>, doi:10.48550/arXiv.1605.08803.

Eskicioglu, A., Fisher, P., 1995. Image quality measures and their performance. *IEEE Transactions on Communications* 43, 2959–2965. doi:10.1109/26.477498.

Gehring, M., Tomaszewski, M., McIntyre, D., Disselhorst, J., Bohndiek, S., 2020. Co-registration of optoacoustic tomography and magnetic resonance imaging data from murine tumour models. *Photoacoustics* 18, 100147. doi:10.1016/j.pacs.2019.100147.

Haghighat, M.B.A., Aghagolzadeh, A., Seyedarabi, H., 2011. A non-reference image fusion metric based on mutual information of image features. *Computers and Electrical Engineering* 37, 744–756. doi:10.1016/j.compeleceng.2011.07.012.

Han, Y., Cai, Y., Cao, Y., Xu, X., 2013a. A new image fusion performance metric based on visual information fidelity. *Information Fusion* 14, 127–135. doi:10.1016/j.inffus.2011.08.002.

Han, Z., Tang, X., Gao, X., Hu, F.Z., 2013b. Image fusion and image quality assessment of fused images. *The International Archives of the Photogrammetry, Remote Sensing and Spatial Information Sciences XL-7/W1*, 33–36. doi:10.5194/isprsarchives-xl-7-w1-33-2013.

He, K., Zhang, X., Ren, S., Sun, J., 2016. Deep residual learning for image recognition. 2016 IEEE Conference on Computer Vision and Pattern Recognition (CVPR), 770–778doi:10.1109/cvpr.2016.90.

Hu, Y., Lafci, B., Luzgin, A., Wang, H., Klohs, J., Deán-Ben, X.L., Ni, R., Razansky, D., Ren, W., 2021. Deep learning facilitates fully automated brain image registration of optoacoustic tomography and magnetic resonance imaging. *Biomedical Optics Express* 13, 4817–4817. doi:10.1364/boe.458182.

Huda, K., Lawrence, D.J., Thompson, W., Lindsey, S.H., Bayer, C.L., 2023. In vivo noninvasive systemic myography of acute systemic vasoactivity in female pregnant mice. *Nature communications* 14. doi:10.1038/s41467-023-42041-8.

Lauri, A., Soliman, D., Omar, M., Stelzl, A., Ntziachristos, V., Westmeyer, G.G., 2019. Whole-cell photoacoustic sensor based on pigment relocation. *ACS Sensors* 4, 603–612. doi:10.1021/acssensors.8b01319.

Li, H., Wu, X.J., 2019. Densefuse: A fusion approach to infrared and visible images. *IEEE Transactions on Image Processing* 28, 2614–2623. doi:10.1109/tip.2018.2887342.

Li, H., Wu, X.J., Durrani, T., 2020a. Nestfuse: An infrared and visible image fusion architecture based on nest connection and spatial/channel attention models. *IEEE Transactions on Instrumentation and Measurement* 69, 9645–9656. doi:10.1109/tim.2020.3005230.

Li, H., Wu, X.J., Kittler, J., 2018a. Infrared and visible image fusion using a deep learning framework. 2018 24th International Conference on Pattern Recognition (ICPR), 2705–2710URL: <https://ieeexplore.ieee.org/document/8546006>, doi:10.1109/ICPR.2018.8546006.

Li, H., Wu, X.J., Kittler, J., 2020b. Mdlatlr: A novel decomposition method for infrared and visible image fusion. *IEEE Transactions on Image Processing* 29, 4733–4746. doi:10.1109/tip.2020.2975984.

Li, W., Xie, Y., Zhou, H., Han, Y., Zhan, K., 2018b. Structure-aware image fusion. *Optik* 172, 1–11. URL: <https://www.sciencedirect.com/science/article/abs/pii/S003040261830932X>, doi:10.1016/j.ijleo.2018.06.123.

Liang, Z., Zhang, S., Wu, J., Li, X., Zhuang, Z., Feng, Q., Chen, W., Li, Q., 2022. Automatic 3-d segmentation and volumetric light fluence correction for photoacoustic tomography based on optimal 3-d graph search. *Medical Image Analysis* 75, 102275–102275. doi:10.1016/j.media.2021.102275.

Lin, L., Hu, P., Tong, X., Na, S., Cao, R., Yuan, X., Garrett, D., Shi, J., Maslov, K., Wang, L.V., 2021. High-speed three-dimensional photoacoustic computed tomography for preclinical research and clinical translation. *Nature Communications* 12. doi:10.1038/s41467-021-21232-1.

Liu, Y., Chen, X., Cheng, J., Peng, H., Wang, Z., 2018. Infrared and visible image fusion with convolutional neural networks. *International Journal of Wavelets, Multiresolution and Information Processing* 16, 1850018. doi:10.1142/s0219691318500182.

Liu, Y., Jin, J., Wang, Q., Shen, Y., Dong, X., 2014. Region level based multi-focus image fusion using quaternion wavelet and normalized cut. *Signal processing* 97, 9–30. doi:10.1016/j.sigpro.2013.10.010.

Ma, J., Chen, C., Li, C., Huang, J., 2016. Infrared and visible image fusion via gradient transfer and total variation minimization. *Information Fusion* 31, 100–109. doi:10.1016/j.inffus.2016.02.001.

Ma, J., Tang, L., Xu, M., Zhang, H., Xiao, G., 2021. Stdffusionnet: An infrared and visible image fusion network based on salient target detection. *IEEE Transactions on Instrumentation and Measurement* 70, 1–13. doi:10.1109/tim.2021.3075747.

Ma, J., Xu, H., Jiang, J., Mei, X., Zhang, X.P., 2020. Ddcgan: A

- dual-discriminator conditional generative adversarial network for multi-resolution image fusion. *IEEE Transactions on Image Processing* 29, 4980–4995. doi:10.1109/tip.2020.2977573.
- Ma, J., Zhou, Z., Wang, B., Zong, H., 2017. Infrared and visible image fusion based on visual saliency map and weighted least square optimization. *Infrared Physics and Technology* 82, 8–17. doi:10.1016/j.infrared.2017.02.005.
- Naidu, V., 2011. Image fusion technique using multi-resolution singular value decomposition. *Defence Science Journal* 61, 479. doi:10.14429/dsj.61.705.
- Ni, R., Deán-Ben, X.L., Treyer, V., GIETL, A., Hock, C., Klohs, J., Nitsch, R.M., Razansky, D., 2022. Coregistered transcranial optoacoustic and magnetic resonance angiography of the human brain. *Optics Letters* 48, 648–648. doi:10.1364/ol.475578.
- Ni, R., Rudin, M., Klohs, J., 2018a. Cortical hypoperfusion and reduced cerebral metabolic rate of oxygen in the  $\alpha/\beta$  mouse model of alzheimer's disease. *Photoacoustics* 10, 38–47. doi:10.1016/j.pacs.2018.04.001.
- Ni, R., Vaas, M., Ren, W., Klohs, J., 2018b. Noninvasive detection of acute cerebral hypoxia and subsequent matrix-metalloproteinase activity in a mouse model of cerebral ischemia using multispectral-optoacoustic tomography. *Neurophotonics* 5, 1. doi:10.1117/1.nph.5.1.015005.
- Qu, G., Zhang, D., Yan, P., 2002. Information measure for performance of image fusion. *Electronics Letters* 38, 313. doi:10.1049/e1:20020212.
- Ren, W., Deán-Ben, X.L., Augath, M.A., Razansky, D., 2021. Development of concurrent magnetic resonance imaging and volumetric optoacoustic tomography: A phantom feasibility study. *Journal of Biophotonics* 14. doi:10.1002/jbio.202000293.
- Sajjadi, M.S.M., Scholkopf, B., Hirsch, M., 2017. Enhancenet: Single image super-resolution through automated texture synthesis. 2017 IEEE International Conference on Computer Vision (ICCV) doi:10.1109/iccv.2017.481.
- Sandler, M., Howard, A., Zhu, M., Zhmoginov, A., Chen, L.C., 2018. Mobilenetv2: Inverted residuals and linear bottlenecks. 2018 IEEE/CVF Conference on Computer Vision and Pattern Recognition doi:10.1109/cvpr.2018.00474.
- Simonyan, K., Zisserman, A., 2015. Very deep convolutional networks for large-scale image recognition. *International Conference on Learning Representations (ICLR)* URL: <https://arxiv.org/abs/1409.1556>.
- Sun, M., Li, C., Chen, N., Zhao, H., Ma, L., Liu, C., Shen, Y., Lin, R., Gong, X., 2020. Full three-dimensional segmentation and quantification of tumor vessels for photoacoustic images. *Photoacoustics* 20, 100212. URL: <https://www.sciencedirect.com/science/article/pii/S2213597920300525>, doi:10.1016/j.pacs.2020.100212.
- Viola, P., Wells, W.M., 1995. Alignment by maximization of mutual information. *International Conference on Computer Vision* doi:10.1109/iccv.1995.466930.
- Wang, L.V., Hu, S., 2012. Photoacoustic tomography: In vivo imaging from organelles to organs. *Science* 335, 1458–1462. doi:10.1126/science.1216210.
- Wang, L.V., Yao, J., 2016. A practical guide to photoacoustic tomography in the life sciences. *Nature Methods* 13, 627–638. doi:10.1038/nmeth.3925.
- Wang, Z., Wang, Z., Zheng, Y., Chuang, Y.Y., Satoh, S., 2019. Learning to reduce dual-level discrepancy for infrared-visible person re-identification. *Computer Vision and Pattern Recognition* doi:10.1109/cvpr.2019.00071.
- Wu, Z., Liu, Z., Lin, J., Lin, Y., Han, S., 2020. Lite transformer with long-short range attention. *International Conference on Learning Representations (ICLR)*.
- Xu, H., Ma, J., Jiang, J., Guo, X., Ling, H., 2022. U2fusion: A unified unsupervised image fusion network. *IEEE Transactions on Pattern Analysis and Machine Intelligence* 44, 502–518. doi:10.1109/tpami.2020.3012548.
- Xu, H., Ma, J., Zhang, X.P., 2020. Mef-gan: Multi-exposure image fusion via generative adversarial networks. *IEEE Transactions on Image Processing* 29, 7203–7216. doi:10.1109/tip.2020.2999855.
- Xydeas, C., Petrovic, V., 2000. Objective image fusion performance measure. *Electronics Letters* 36, 308. doi:10.1049/e1:20000267.
- Yang, B., Li, S., Sun, F., 2007. Image fusion using nonsubsampled contourlet transform doi:10.1109/icig.2007.124.
- Yuan, Z., Jiang, H., 2006. Quantitative photoacoustic tomography: Recovery of optical absorption coefficient maps of heterogeneous media. *Applied Physics Letters* 88, 231101. doi:10.1063/1.2209883.
- Zamir, S.W., Arora, A., Khan, S., Hayat, M., Khan, F.S., Yang, M.H., 2022. Restormer: Efficient transformer for high-resolution image restoration doi:10.1109/cvpr52688.2022.00564.
- Zhang, H., Yuan, J., Tian, X., Ma, J., 2021a. Gan-fm: Infrared and visible image fusion using gan with full-scale skip connection and dual markovian discriminators. *IEEE Transactions on Computational Imaging* 7, 1134–1147. URL: <https://ieeexplore.ieee.org/document/9573457>, doi:10.1109/TCI.2021.3119954.
- Zhang, S., Li, Q., Li, X., Liang, Z., Sun, X., Liu, J., Lu, L., Feng, Y., Chen, W., 2022. Mri information-based correction and restoration of photoacoustic tomography. *IEEE Transactions on Medical Imaging* 41, 2543–2555. doi:10.1109/tmi.2022.3165839.
- Zhang, S.N., Lv, Q., Li, X., Liang, Z., Wu, J., Huang, S., Liu, J.B., Zhuang, Z., Feng, Y., Feng, Q., Chen, W., 2021b. In vivo co-registered hybrid-contrast imaging by successive photoacoustic tomography and magnetic resonance imaging. *bioRxiv (Cold Spring Harbor Laboratory)* doi:10.1101/2021.03.06.434031.
- Zhang, Y., Liu, Y., Sun, P., Yan, H., Zhao, X., Zhang, L., 2020. Ifcnn: A general image fusion framework based on convolutional neural network. *Information Fusion* 54, 99–118. doi:10.1016/j.inffus.2019.07.011.
- Zhang, Y., Zhang, L., Bai, X., Zhang, L., 2017. Infrared and visual image fusion through infrared feature extraction and visual information preservation. *Infrared Physics and Technology* 83, 227–237. doi:10.1016/j.infrared.2017.05.007.
- Zhong, Y., Zhang, S., Liu, Z., Zhang, X., Mo, Z., Zhang, Y., Hu, H., Chen, W., Li, Q., 2024. Unsupervised fusion of misaligned pat and mri images via mutually reinforcing cross-modality image generation and registration. *IEEE Transactions on Medical Imaging*, 1–1doi:10.1109/tmi.2023.3347511.
- Zhou, Z., Li, S., Wang, B., 2014. Multi-scale weighted gradient-based fusion for multi-focus images. *Information Fusion* 20, 60–72. doi:10.1016/j.inffus.2013.11.005.
- Zhu, J.Y., Park, T., Isola, P., Efros, A.A., 2017. Unpaired image-to-image translation using cycle-consistent adversarial networks. 2017 IEEE International Conference on Computer Vision (ICCV) doi:10.1109/iccv.2017.244.